Preprints.org

Article

Channel Estimation in UAV-Assisted OFDM Systems by Leveraging LoS and Echo Sensing with Carrier Aggregation

Zhuolei Chen [*] , Wenbin Wu [*] , Renshu Wang , Manshu Liang , Weihao Zhang , Shuning Yao , Wenquan Hu , Chaojin Qing

Article

Channel Estimation in UAV-Assisted OFDM Systems by Leveraging LoS and Echo Sensing with Carrier Aggregation

Zhuolei Chen [1,*], **Wenbin Wu** [1,*], **Renshu Wang** [1], **Manshu Liang** [1], **Weihao Zhang** [1], **Shuning Yao** [1], **Wenquan Hu** [2] **and Chaojin Qing** [2]

[1] Electric Power Research Institute of State Grid Fujian Electric Power Co., Ltd, Fujian, 350007, China
[2] School of Electrical Engineering and Electronic Information, Xihua University, Chengdu 610039, China
[*] Correspondence: wenbinwu@vip.qq.com (Z.C.); dky_czl@163.com (W.W.)

Abstract

Unmanned aerial vehicle (UAV)-assisted wireless communication systems often employ the carrier aggregation (CA) technique to alleviate the issue of insufficient bandwidth. However, in high-mobility UAV communication scenarios, the dynamic channel characteristics pose significant challenges to channel estimation (CE). Given these challenges, integrated sensing and communication (ISAC), which combines communication and sensing functionalities, has emerged as a promising solution to enhance CE accuracy for UAV systems. Meanwhile, the dominant line-of-sight (LoS) characteristics inherent in UAV scenarios present a valuable opportunity for further exploitation. To this end, this paper proposes a LoS and echo sensing-based CE scheme for CA-enabled UAV-assisted communication systems. Firstly, LoS sensing and echo sensing techniques are employed to acquire sensing-assisted prior information. Subsequently, the obtained prior information is utilized to refine the CE of the primary component carrier (PCC) in CA, thereby improving the accuracy of channel parameter estimation for the PCC. Based on the path-sharing property between PCC and secondary component carriers (SCCs), a three-stage scheme is proposed to reconstruct the channel of SCCs. In Stages I and II, the path-sharing property is exploited to reconstruct the LoS and non-line-of-sight (NLoS) paths of the SCCs in the delay-Doppler (DD) domain, respectively. Finally, an iterative procedure is applied to enhance the initial reconstruction and further recover non-shared transmission paths between PCC and SCCs. Simulation results demonstrate that the proposed method effectively enhances the CE accuracy for both PCC and SCCs. Furthermore, the proposed scheme exhibits robustness against parameter variations.

Keywords: unmanned aerial vehicle (UAV); channel estimation (CE); carrier aggregation (CA); integrated sensing and communication (ISAC); delay-Doppler (DD)

---

1. Introduction

1.1. Background

Unmanned aerial vehicles (UAVs) have been widely deployed in numerous civil applications such as power inspection, disaster rescue, agricultural monitoring, and logistics delivery, as well as specialized scenarios including military reconnaissance, owing to their advantages in flexible deployment, high mobility, and extensive coverage [1,2]. With the evolution from 5G to 6G, UAV-assisted communication systems, which enable rapid deployment of temporary communication infrastructures and enhanced coverage quality, have become a critical component of space-air-ground-sea integrated network [3]. In UAV-assisted communication systems, the performance of communication links is directly determined by the accuracy of channel estimation (CE), thereby affecting flight safety and mission completion [4–7]. On the one hand, the high mobility of UAVs results in rapid time-varying

channels. On the other hand, applications such as high-definition video transmission and multi-UAV coordination impose more stringent requirements for system bandwidth [8]. Notably, UAV-assisted communication systems exhibit dominant Line-of-Sight (LoS) links and echo-based sensing information. The exploitation of these characteristics and sensing information offers significant potential to mitigate the impact of rapid channel variations caused by high UAV mobility. To address the issue of bandwidth demand, carrier aggregation (CA) technology efficiently integrates discrete spectrum resources [9–12]. It not only enhances the capacity of UAV-assisted communication systems, but also provides opportunities for developing LoS and echo sensing information-based CE methods.

1.2. Related Works

In UAV-assisted communication systems, orthogonal frequency division multiplexing (OFDM) modulation has attracted significant attention due to its robust ability to mitigate multipath interference [5–7,13]. For UAV-assisted OFDM systems, considerable research has been conducted on CE for ground base stations (gBS) [5–7,14–17]. In [5], tailored tensor models are employed across different UAV-assisted communication scenarios to achieve joint CE and symbol detection (SD). To enhance bandwidth efficiency in OFDM-based UAV communication systems operating in time-varying environments, a deep learning-based pilot-free approach for joint channel and carrier frequency offset equalization is proposed in [6]. Meanwhile, a multi-resolution deep neural network-based CE method is proposed in [7] for UAV-assisted OFDM systems to enhance both computational efficiency and prediction performance. To address the beam squint issue in high-frequency bands, a gridless compressed sensing (CS)- based CE method is proposed for UAV-assisted communications in [14]. For massive multiple-input multiple-output (MIMO) UAV-assisted communication systems with a single radio frequency chain architecture, a hybrid parametric/non-parametric CE scheme incorporating UAV state-space information is proposed in [15]. While the aforementioned methods offer valuable insights into CE for UAV-assisted OFDM systems, they generally overlook the dominant LoS characteristics inherent in UAV scenarios. Inspired by integrated sensing and communication (ISAC), a LoS sensing-enhanced CE method was proposed in [16] for UAV-assisted OFDM systems to improve estimation accuracy by applying a denoising threshold for LoS/non-line-of-sight (NLoS) detection. For UAV emergency communications, a pilot-based ISAC system was developed in [17], which enhances communication reliability while simultaneously achieving superior ranging accuracy compared to conventional schemes. Although prior studies have explored ISAC-enabled UAV communication designs [18–20], research on sensing-assisted CE schemes remains limited, impeding further enhancement of CE accuracy in UAV-assisted OFDM systems.

In ISAC systems, several studies have focused on leveraging sensing-based parameters to enhance the CE performance [21–30]. In [21], roadside units employ ISAC signals to serve downlink information transmission and channel parameter prediction. This approach designs a downlink beamforming to mitigate channel interference, thereby enabling vehicles to directly detect information without performing CE. To address the lack of signal processing capability at an intelligent reflecting surface (IRS) as well as the mutual interference between sensing and communication signals, a deep learning-based approach is explored in [22] for CE in IRS-assisted ISAC systems. By leveraging joint burst sparsity and pilot beamforming gain, a two-stage joint scheme for beam steering optimization, target detection, and CE is proposed in [23], enhancing both detection and estimation performance. To reduce communication overhead and enhance efficiency, the application potential of extreme learning machines in IRS-assisted multiuser ISAC systems is demonstrated in [24]. In [25], a closed-form solution for minimum mean square error (MMSE) CE is derived under constraints of communication CE and radar ambiguity function, by leveraging reference signals for radar sensing. Leveraging the correlation between channel and sensing, a sensing-assisted Kalman filtering-based approach for channel state information (CSI) estimation is proposed in [26], which improves CSI accuracy through angle-of-arrival (AoA) estimation. For MIMO-OFDM ISAC systems, an angle-subspace-based CSI refinement and angle-domain optimization scheme for angle-of-departure (AoD) estimation is introduced in [27]. To enhance uplink communication performance by leveraging sensing parameters,

the work in [28] formulates CE and SD as a constrained bilinear recovery problem and develops a bilinear unitary approximate message passing algorithm to solve it. For orthogonal time frequency space modulation, a sparse Bayesian learning algorithm is proposed to improve CE accuracy by exploiting the joint sparsity between sensing and communication channels [29]. To reduce beam training overhead and improve communication throughput, reference signals are utilized in [30] for sensing-assisted beam management, simultaneously accelerating beam failure detection and recovery procedures. Furthermore, to fully exploit the rich echo information in wireless environments, a communication echo sensing-assisted CE method is proposed in [31]. These methods provide valuable insights for CE in UAV-assisted OFDM systems. However, they have not adequately incorporated the dominant LoS characteristics inherent in UAV-assisted communication scenarios.

CA technology represents a promising solution for enhancing data transmission bandwidth in UAV-assisted OFDM systems. Several studies have investigated CE methods in CA-enabled wireless communication systems [32–34]. Specifically, the time-frequency channel correlation across different component carriers (CCs) in OFDM systems is exploited to improve CE accuracy [32]. In [33], a subchannel selection strategy for CA-OFDM systems is developed based on the analysis of CE error. In UAV-assisted CA-OFDM systems, employing adaptive pilot interval and power allocation for CE achieves both performance improvement and reduced pilot overhead [34]. In [35], a CA experimental testbed is developed to evaluate the CE performance of spectrum-efficient frequency division multiplexing and OFDM systems. Furthermore, an interleaved pilot structure based on CA is proposed in [36] for enhanced ISAC signal design and sensing performance, demonstrating its advantages in CA-enabled ISAC systems. Incorporating CA technology effectively meets the high-bandwidth requirements in UAV-assisted OFDM systems, thereby enabling applications such as real-time video transmission, multi-UAV cooperative operations, and complex environmental sensing.

1.3. Motivation and Contributions

As previously discussed, CE in UAV-assisted OFDM systems still faces challenges such as inadequate exploitation of channel characteristics, underutilization of sensing information, and inability to meet high-bandwidth demands. To address these issues, this paper proposes a LoS and echo sensing-aided CE method for UAV-assisted OFDM systems with CA technology. The contributions of this paper are summarized as follows:

1. We propose a prior information extraction method by leveraging LoS and echo sensing. In this method, the LoS sensing technology is employed to acquire the prominent LoS characteristics in UAV communication scenarios. Furthermore, based on echo sensing signals, this method incorporates radar signal processing technology to extract channel prior information. By integrating both LoS and echo sensing, we derive enhanced prior information to assist and refine CE.
2. Based on the extracted LoS and echo sensing prior information, we propose a LoS and echo sensing-aided CE method for CA-enabled UAV-assisted OFDM systems. This method utilizes the sensed LoS component as a reference for setting detection threshold in CE, while incorporating echo-based sensing information to suppress noise and interference from false paths. By jointly leveraging LoS and echo sensing, an adaptive threshold for detecting transmission paths is designed, which is beneficial for enhancing CE accuracy.
3. By leveraging the LoS path characteristics, we propose a path sharing-based channel reconstruction scheme. In this scheme, the PCC assists in reconstructing the channels of SCCs. This scheme exploits the shared transmission paths between the PCC and SCCs by utilizing Doppler-domain information to aid the reconstruction of the LoS path for SCCs. Furthermore, this reconstruction scheme is extended to NLoS paths, forming a three-stage channel reconstruction framework for SCCs. Consequently, the pilot overhead required for CE of SCCs is effectively reduced, thereby increasing the overall data transmission rate of CA systems.

1.4. Outline and Notation

The remainder of this paper is organized as follows: Section 2 introduces the signal model for CA communications and the system model for echo sensing. Section 3 elaborates on the proposed LoS and echo sensing-assisted CA-CE method. Numerical results are presented in Section 4. Finally, Section 5 concludes the paper.

Notations: Boldface smaller case and upper case letters represent vector and matrix, respectively. $(\cdot)^H$ stands for the conjugate transpose. $*$ denotes linear convolution. $\mathbb{E}(\cdot)$ denotes the complex expectation operation. $\delta(\cdot)$ represents the Dirac delta function. The circularly symmetric Gaussian distribution with mean ω and variance σ^2 is denoted by $\mathcal{CN}(\omega, \sigma^2)$, and $\sim$ stands for "distributed as". $\|\cdot\|_2^2$ is the Euclidean norm. $\mathbf{F}_N$ is the N-point normalized $N \times N$ discrete Fourier transform (DFT) matrix. $\lceil x \rceil$ denotes the ceiling operation on x. $\mathbb{C}^{M \times N}$ denotes $M \times N$ dimensional complex matrices. $\cap$ denotes the intersection set.

2. System Model

This section presents the system model utilized in this paper. Specifically, Section 2.1 introduces the communication model based on CA-OFDM while Section 2.2 describes the echo sensing model.

2.1. CA-OFDM Communication Model

The UAV-assisted OFDM system with CA is considered in this paper, which employs B component carriers (CCs) and M subcarriers. At the transmitter, an inverse discrete Fourier transform (IDFT) is applied to transform the data/pilot symbol $X_b(m)$ (with $b = 1, 2, \cdots, B$) on the m-th subcarrier (with $m = 0, 1, \cdots, M-1$) of the b-th CC into the time domain $x_b(n)$ (with $n = 0, 1, \cdots, M-1$), which is expressed as [32,37]

$$x_b(n) = \frac{1}{M} \sum_{m=0}^{M-1} X_b(m) \exp\left(j2\pi \frac{nm}{M}\right). \tag{1}$$

According to [16] and [32], after appending a cyclic prefix (CP), the time-domain transmitted signal $x_{b,\text{CP}}(n)$ of the b-th CC is given by

$$x_{b,\text{CP}}(n) = \begin{cases} x_b(n+N), & n = -L_{\text{CP}}, \ldots, -1 \\ x_b(n), & n = 0, 1, \ldots, N-1 \end{cases}, \tag{2}$$

where L_{CP} denotes the length of CP. At the receiver, the received signal $y_{b,\text{CP}}(n)$ of the b-th CC is expressed as [32]

$$y_{b,\text{CP}}(n) = x_{b,\text{CP}}(n) * h_b(n) + w_b(n), \tag{3}$$

where $h_b(n)$ represents the channel impulse response (CIR) of the b-th CC, and $w_b(n)$ denotes additive white Gaussian noise (AWGN) with zero mean and variance σ_w^2. According to [16], the CIR of the b-th CC, denoted as $h_b(n)$, is given by

$$h_b(n) = \underbrace{\sqrt{\frac{\mathcal{K}}{\mathcal{K}+1}} h_{0,b} \delta(n - \tau_{0,b})}_{\triangleq h_{\text{LoS}}} + \underbrace{\sqrt{\frac{1}{\mathcal{K}+1}} \sum_{l=1}^{L-1} h_{l,b} \delta(n - \tau_{l,b})}_{\triangleq h_{\text{NLoS}}}, \tag{4}$$

where $\mathcal{K}$ denotes the Rician factor, $h_{0,b}$ and $\tau_{0,b}$ represent the channel gain and path delay of the LoS component for the b-th CC, respectively. $h_{l,b}$ and $\tau_{l,b}$ correspond to the channel gain and path delay of the NLoS components for the b-th CC, respectively. $\delta(\cdot)$ denotes the Dirac delta function. In this paper, the time-varying fading coefficient $h_{l,b}$ is modeled as a zero-mean Gaussian process following the Jakes Doppler spectrum with independent transmission paths [30].

Without loss of generality, the length of the CP L_{CP} is chosen to be larger than that of the CIR to prevent inter-symbol interference (ISI), i.e., $L_{\text{CP}} > L$ [16,32]. At the transmitter, the transmitted wireless data frame consists of D OFDM symbols. After removing the CP and applying the discrete

Fourier transform (DFT), the equivalent baseband signal $Y_b(m,d)$ on the m-th subcarrier of the d-th symbol (with $d = 0, 1, \cdots, D-1$) for the b-th CC at the ground base station (gBS) receiver is expressed as [31,37]

$$Y_b(m,d) = H_b(m,d)X_b(m,d) + W_b(m,d), \tag{5}$$

where $H_b(m,d)$, $X_b(m,d)$, and $W_b(m,d)$ denote the channel frequency response (CFR), the transmitted data/pilot symbol, and the AWGN term with zero mean and variance σ_w^2, respectively, for the m-th subcarrier of the d-th symbol for the b-th CC. Based on the received signal $Y_b(m,d)$, the initial CFR is obtained using a classical CE method, such as the least squares (LS) approach. Subsequently, sensing-aided prior information is utilized to refine or reconstruct the initial CFR.

2.2. Echo Sensing Model

In next-generation wireless communication systems, echo signals, previously regarded as interference or noise, are now recognized as a valuable source of sensing information and have become one of the key enablers for ISAC designs [31,38]. To this end, this paper explores the extraction of sensing information from echo signals at the gBS.

The transmitted signal comprises K OFDM symbols, each containing S subcarriers. At the gBS transmitter, after performing the IDFT operation and CP insertion, the transmitted signal in the time domain, denoted as $x_{\text{Sen}}(t)$, is expressed as [39–41]

$$x_{\text{Sen}}(t) = \sum_{k=0}^{K-1} \sum_{s=0}^{S-1} X_{\text{Sen}}(k,s) e^{j2\pi s \Delta f t} g(t - kT_o), \tag{6}$$

where $X_{\text{Sen}}(k,s)$ with $k = 0, 1, \cdots, K-1$ and $s = 0, 1, \cdots, S-1$ denotes the transmitted symbol on the s-th subcarrier of the k-th OFDM symbol, Δf represents the subcarrier spacing, T_o denotes the duration of an OFDM symbol (including the CP duration T_c and the symbol duration T_d), and $g(\cdot)$ represents the rectangular pulse function. To prevent ISI, the duration of the CP, denoted as T_c, is configured to be longer than both the maximum multipath delay and the delay corresponding to the maximum detectable range [31,39]. At the gBS receiver, the echo signal $y_{\text{Sen}}(t)$ received through P propagation paths is expressed as [31,39]

$$y_{\text{Sen}}(t) = \sum_{p=1}^{P} \sum_{k=0}^{K-1} \sum_{s=0}^{S-1} \alpha_p X_{\text{Sen}}(k,s) e^{j2\pi s \Delta f \left(t - \tau_p\right)} e^{j2\pi f_{D,p} t} g\left(t - kT_o - \tau_p\right) + w(t), \tag{7}$$

where α_p, τ_p, and $f_{D,p}$ denote the amplitude, delay, and Doppler shift of the $p(p = 1, 2, \cdots, P)$-th path, respectively, and $w(t)$ represents the AWGN with zero mean and variance σ_w^2. After CP removal, the received echo signal $y_{\text{Sen}}(t)$ is transformed into the frequency domain, denoted as $Y_{\text{Sen}}(k,s)$, yielding [39,40]

$$Y_{\text{Sen}}(k,s) = \sum_{p=1}^{P} \alpha_p X_{\text{Sen}}(k,s) e^{-j2\pi s \Delta f \tau_p} e^{j2\pi k T_o f_{D,p}} + W(k,s), \tag{8}$$

where $W(k,s)$ represents the AWGN on the s-th subcarrier of the k-th OFDM symbol. Then, the radar signal processing techniques, such as 2D fast Fourier transform (FFT) [39] and 2D multiple signal classification (MUSIC) [40], are employed to extract sensing information from the received echo signal $Y_{\text{Sen}}(k,s)$.

3. LoS and Echo Sensing-aided CE

The LoS and echo sensing-aided CE is elaborated in this section. In Section 3.1, we introduce the LoS sensing method and the extraction of echo sensing-assisted prior information. Based on the extracted LoS and echo sensing information, Section 3.2 elaborates the process of PCC CE enhancement. By leveraging the LoS path-sharing mechanism between the PCC and SCCs, Section 3.3 reconstructs

the SCC channel by utilizing the path information from both PCC and SCCs, and further develops a sensing-assisted iteration scheme to enhance the reconstruction accuracy.

3.1. Sensing Information Extraction

3.1.1. LoS Sensing

In UAV-assisted OFDM systems, the UAV-to-ground (U2G) link exhibits a high probability of LoS propagation [16,42]. Typically, the LoS path is significantly stronger than individual NLoS paths (by approximately 20 dB) [16]. These observations highlight both the prevalence and detectability of LoS components in U2G links, thus motivating the exploitation of these components to improve CE accuracy. Based on the CIR, the presence of a LoS path is detected using the kurtosis of the received power. By denoting the kurtosis as κ, we have [16]

$$\kappa = \frac{E\left[\left(|h(\tau)| - \mu_{|h(\tau)|}\right)^4\right]}{\sigma_{|h(\tau)|}^4}, \tag{9}$$

where τ and $h(\tau)$ represent the tap delay and CIR of the transmission path, respectively, while $\mu_{|h(\tau)|}$ and $\sigma_{|h(\tau)|}$ denote the mean and standard deviation of $h(\tau)$. Due to the notably higher kurtosis value in LoS scenarios compared to NLoS conditions, the presence of a LoS path can be effectively detected when the computed value of κ exceeds a predefined threshold [16]. In this paper, the kurtosis-based detection of the received power is used as an example to demonstrate the feasibility of LoS sensing via received signals. It is noteworthy that other LoS sensing methods are equally applicable, though not elaborated here.

3.1.2. Echo Sensing Information Extraction

By utilizing the received signal $Y_{\text{Sen}}(k,s)$ from Eq. (8) and the known transmitted signal $X_{\text{Sen}}(k,s)$, the channel transfer function of the echo signal is derived. By denoting the transfer function as $H_{\text{Sen}}(k,s)$, we have [31]

$$H_{\text{Sen}}(k,s) = \frac{Y_{\text{Sen}}(k,s)}{X_{\text{Sen}}(k,s)} = \sum_{p=1}^{P} \alpha_p e^{-j2\pi s \Delta f \tau_p} e^{j2\pi k T_o f_{D,p}} + \overline{W}(k,s), \tag{10}$$

where $\overline{W}(k,s)$ represents AWGN satisfying $\overline{W}(k,s) \sim \mathcal{CN}\left(0, \sigma_{\text{Sen}}^2\right)$, and σ_{Sen}^2 denotes the noise variance. Then, the delay-Doppler (DD) periodogram $G_{\text{Sen}}(v,q)$ is obtained by applying the 2D FFT, which is given by [31]

$$
\begin{aligned}
G_{\text{Sen}}(v,q) &= \frac{1}{K} \sum_{k=0}^{K-1} \sum_{s=0}^{S-1} H_{\text{Sen}}(k,s) e^{j2\pi\left(\frac{s}{S}v - \frac{k}{K}q\right)} \\
&\approx \frac{1}{K} \sum_{k=0}^{K-1} \sum_{s=0}^{S-1} \sum_{p=1}^{P} \alpha_p e^{j2\pi\left(\frac{s}{S}v + kT_o f_{D,p} - \frac{k}{K}q - s\Delta f \tau_p\right)'}
\end{aligned} \tag{11}
$$

where $v = 0, 1, \cdots, K-1$ and $q = 0, 1, \cdots, S-1$. Based on the 2D periodogram, the delay and Doppler shift parameters of resolvable paths are estimated using a 2D cell-averaging constant false alarm rate (CA-CFAR) detector [31]. By representing the set of indices for the reference cells in the reference window as $\mathcal{R}$, the average power $\overline{\beta}$ is then given by [31]

$$\overline{\beta} = \frac{1}{N_g} \sum_{(v,q) \in \mathcal{R}} |G_{\text{Sen}}(v,q)|^2, \tag{12}$$

where N_g denotes the number of reference cells in set $\mathcal{R}$. The detection threshold T_{h} is then constructed as [31]

$$T_{\text{h}} = N_g \left(P_f^{-1/N_g} - 1\right) \cdot \overline{\beta}, \tag{13}$$

where P_f is the predefined false alarm probability for the 2D CA-CFAR detector. Based on the detection threshold T_h, a hypothesis test is formulated as follows

$$|G_{ES}(\widehat{v},\widehat{q})|^2 \underset{\mathcal{H}_0}{\overset{\mathcal{H}_1}{\gtrless}} T_h, \tag{14}$$

where the index of the cell under test is denoted by $(\widehat{v},\widehat{q})$, and $\mathcal{H}_1$ and $\mathcal{H}_0$ represent the hypotheses of the presence and absence of an echo path, respectively. After detecting all peaks in the DD periodogram, a set $\mathcal{I}$ of sensing information is formed. The number of resolvable echo paths, denoted by G, is determined by the cardinality of set $\mathcal{I}$, i.e., $G = \|\mathcal{I}\|_0$. Accordingly, the sensing information set $\mathcal{I}$ indexed by $(\widehat{v}_g, \widehat{q}_g)$ with $g = 1, 2, \cdots, G$ is expressed as

$$\mathcal{I} \triangleq \left\{ \widehat{\tau}_g = \frac{\widehat{v}_g}{K\Delta f}, \widehat{f}_{D,g} = \frac{\widehat{q}_g}{ST_o} \right\}_{g=1,2,\cdots,G}, \tag{15}$$

where $\widehat{\tau}_g$ and $\widehat{f}_{D,g}$ denote the delay and Doppler shift of the echo path indexed by $(\widehat{v}_g, \widehat{q}_g)$, respectively. Notably, not all detected echo paths in the sensing-derived information set $\mathcal{I}$ correspond to those from the UAV. As the primary focus of this work is to enhance UAV communication CE using echo sensing, methods for false alarm suppression [31] are not discussed in detail. As such, the sensing information set $\mathcal{I}$ considered herein is assumed to have undergone false path suppression.

3.2. CE Enhancement for PCC

Based on the received signal $Y_b(m,d)$ given in Eq. (5), its time-frequency domain matrix representation $\mathbf{Y}_b \in \mathbb{C}^{M \times D}$ is obtained. By denoting the transmitted pilot signal as $\mathbf{X}_{b,P} \in \mathbb{C}^{M_1 \times N_1}$, the initial CFR $\widehat{\mathbf{H}}_{b,P}^{LS} \in \mathbb{C}^{M_1 \times N_1}$ is estimated using the classical LS method. Its (m_1, n_1)-th element, denoted as $\widehat{H}_{b,P}^{LS}(m_1, n_1)$, is given by

$$\widehat{H}_{b,P}^{LS}(m_1, n_1) = \frac{Y_{b,P}(m_1, n_1)}{X_{b,P}(m_1, n_1)}, \tag{16}$$

where $Y_{b,P}(m_1, n_1)$ represents the element at the m_1-th subcarrier and n_1-th symbol of the received pilot signal matrix $\mathbf{Y}_{P,PCC} \in \mathbb{C}^{M_1 \times N_1}$, and $X_{b,P}(m_1, n_1)$ denotes the element at the m_1-th subcarrier and n_1-th symbol of the transmitted pilot signal matrix $\mathbf{X}_{P,PCC} \in \mathbb{C}^{M_1 \times N_1}$. M_1 and N_1 indicate the number of pilots in the subcarrier direction and the OFDM symbol direction, respectively. Subsequently, linear interpolation is employed to obtain the complete channel matrix $\widehat{\mathbf{H}}^{LS} \in \mathbb{C}^{M \times D}$ in the time-frequency domain.

3.2.1. Sensing-based Prior Information Derivation

Based on the prior information set $\mathcal{I}$ (given by Eq. (15)), the prior information of multipath delays and Doppler shifts is obtained. According to [31], the delay spread σ_τ is calculated as

$$\sigma_\tau = \tau_{max} - \tau_{min} = \underset{\widehat{\tau}_g}{\arg\max}\{\widehat{\tau}_g\} - \underset{\widehat{\tau}_g}{\arg\min}\{\widehat{\tau}_g\}, \tag{17}$$

where τ_{min} and τ_{max} denote the first arrival path delay and the maximum path delay, respectively. Correspondingly, the estimated Doppler spread σ_ν is given by

$$\sigma_\nu = \underset{\widehat{f}_{D,g}}{\arg\max}\left\{\left|\widehat{f}_{D,g}\right|\right\} - \left(-\underset{\widehat{f}_{D,g}}{\arg\max}\left\{\left|\widehat{f}_{D,g}\right|\right\}\right) = 2\underset{\widehat{f}_{D,g}}{\arg\max}\left\{\left|\widehat{f}_{D,g}\right|\right\}. \tag{18}$$

3.2.2. Sensing-aided CE for PCC

It is noteworthy that the delay spread σ_τ and the Doppler spread σ_v exhibit more pronounced characteristics in the DD domain. Therefore, the symplectic finite Fourier transform (SFFT) is employed to transform the initial CFR matrix $\widehat{\mathbf{H}}^{\mathrm{LS}}$ into the DD domain [43], i.e.,

$$\widehat{\mathbf{H}}_{\mathrm{DD}} = \mathbf{F}_M^H \widehat{\mathbf{H}}^{\mathrm{LS}} \mathbf{F}_D, \tag{19}$$

where $\widehat{\mathbf{H}}_{\mathrm{DD}} \in \mathbb{C}^{M \times D}$ denotes the initial channel response in the DD domain. When D is an odd number, $\widehat{\mathbf{H}}_{\mathrm{DD}}$ is expressed as

$$\widehat{\mathbf{H}}_{\mathrm{DD}} = \begin{bmatrix} \widehat{h}_{1,-(D-1)/2} & \cdots & \widehat{h}_{1,-1} & \widehat{h}_{1,0} & \widehat{h}_{1,1} & \cdots & \widehat{h}_{1,(D-1)/2} \\ \widehat{h}_{2,-(D-1)/2} & \cdots & \widehat{h}_{2,-1} & \widehat{h}_{2,0} & \widehat{h}_{2,1} & \cdots & \widehat{h}_{2,(D-1)/2} \\ \vdots & \ddots & \vdots & \vdots & \vdots & \ddots & \vdots \\ \widehat{h}_{M,-(D-1)/2} & \cdots & \widehat{h}_{M,-1} & \widehat{h}_{M,0} & \widehat{h}_{M,1} & \cdots & \widehat{h}_{M,(D-1)/2} \end{bmatrix}, \tag{20}$$

where $\widehat{h}_{j,f}$ with $j \in [1, M]$ and $f \in [-(D-1)/2, (D-1)/2]$ represents the channel response at the (j, f)-th grid in the DD domain. For the case where D is an even number, we have

$$\widehat{\mathbf{H}}_{\mathrm{DD}} = \begin{bmatrix} \widehat{h}_{1,-D/2} & \cdots & \widehat{h}_{1,-1} & \widehat{h}_{1,0} & \widehat{h}_{1,1} & \cdots & \widehat{h}_{1,(D/2)-1} \\ \widehat{h}_{2,-D/2} & \cdots & \widehat{h}_{2,-1} & \widehat{h}_{2,0} & \widehat{h}_{2,1} & \cdots & \widehat{h}_{2,(D/2)-1} \\ \vdots & \ddots & \vdots & \vdots & \vdots & \ddots & \vdots \\ \widehat{h}_{M,-D/2} & \cdots & \widehat{h}_{M,-1} & \widehat{h}_{M,0} & \widehat{h}_{M,1} & \cdots & \widehat{h}_{M,(D/2)-1} \end{bmatrix}, \tag{21}$$

where $f \in [-D/2, D/2 - 1]$. Due to the sparsity of the channel $\widehat{\mathbf{H}}_{\mathrm{DD}}$, a path detection threshold is established using both LoS sensing and echo-based sensing information to fully exploit the channel sparsity. Consequently, the channel response $\widehat{h}_{j,f}$ and the estimated delay spread σ_τ (given in Eq. (17)) and Doppler spread σ_v (given in Eq. (18)) are utilized for noise estimation, which is expressed as

$$\widehat{\sigma}^2 = \begin{cases} \dfrac{\sum\limits_{j=1}^{M} \sum\limits_{f=-(D-1)/2}^{(D-1)/2} \left|\widehat{h}_{j,f}\right|^2 - \sum\limits_{j=1}^{\lceil \sigma_\tau/T_\tau \rceil} \sum\limits_{f=-\lceil \sigma_v/2T_v \rceil}^{\lceil \sigma_v/2T_v \rceil} \left|\widehat{h}_{j,f}\right|^2}{MD - \lceil \sigma_\tau/T_\tau \rceil \cdot (\lceil \sigma_v/T_v \rceil + 1)}, & D \text{ is an odd number} \\[3ex] \dfrac{\sum\limits_{j=1}^{M} \sum\limits_{f=-D/2}^{D/2-1} \left|\widehat{h}_{j,f}\right|^2 - \sum\limits_{j=1}^{\lceil \sigma_\tau/T_\tau \rceil} \sum\limits_{f=-\lceil \sigma_v/2T_v \rceil}^{\lceil \sigma_v/2T_v \rceil} \left|\widehat{h}_{j,f}\right|^2}{MD - \lceil \sigma_\tau/T_\tau \rceil \cdot (\lceil \sigma_v/T_v \rceil + 1)}, & D \text{ is an even number} \end{cases}, \tag{22}$$

where $T_\tau = 1/M \Delta f_{\mathrm{Com}}$ and $T_v = \Delta f_{\mathrm{Com}}/D$ denote the delay resolution and Doppler resolution, respectively, and Δf_{Com} represents the subcarrier spacing of the communication system. According to [31], the detection threshold for CE enhancement, denoted as $\widetilde{T}_{\mathrm{h}}$, is designed by

$$\widetilde{T}_{\mathrm{h}} = \sqrt{-2\widehat{\sigma}^2 \ln P_{\mathrm{fa}}}, \tag{23}$$

where P_{fa} denotes the predefined false alarm probability for detecting transmission paths. Employing $\widetilde{T}_{\mathrm{h}}$ effectively mitigates estimation errors, thereby enhancing CE accuracy. However, $\widetilde{T}_{\mathrm{h}}$ fails to fully capitalize on the sensed LoS path advantage, rendering it vulnerable to multipath interference and degrading the performance of resolvable path detection. To address this limitation, the sensed LoS path is further incorporated to refine the threshold, leading to an enhanced LoS-assisted threshold $T_{\mathrm{h,CE}}$ defined as

$$T_{\mathrm{h,CE}} = \varepsilon \widetilde{T}_{\mathrm{h}}(1 + \delta_{\mathrm{LoS}}), \tag{24}$$

where ε denotes the threshold factor. According to [44], the threshold factor ε is expressed as $\varepsilon = P_{\mathrm{fL}}^{-1/(\beta-1)} - 1$, where P_{fL} and $\beta = \lceil \sigma_\tau/T_\tau \rceil \cdot (\lceil \sigma_v/T_v \rceil + 1)$ represent the false alarm probability based on the LoS threshold and the size of the reference window, respectively. δ_{LoS} represents the path factor

associated with the sensed LoS path. For the estimated DD domain channel response, the path factor δ_{LoS} is given by

$$\delta_{\text{LoS}} = \frac{|h_{\text{LoS}}|}{\sum\limits_{j=1}^{\lceil \sigma_\tau/T_\tau \rceil} \sum\limits_{f=-\lceil \sigma_v/2T_v \rceil}^{\lceil \sigma_v/2T_v \rceil} \left| \widehat{h}_{j,f} \right|^2} + \delta_{\text{noise}}^2, \tag{25}$$

where h_{LoS} denotes the complex gain of the LoS path and δ_{noise}^2 represents the noise factor. Despite the presence of the LoS path, a significant presence of scattered components indicates the existence of NLoS paths, in addition to the inevitable estimation noise at the gBS receiver. Thus, the noise factor δ_{noise}^2 is defined as

$$\delta_{\text{noise}}^2 = \begin{cases} \dfrac{\sum\limits_{j=1}^{M} \sum\limits_{f=-(D-1)/2}^{(D-1)/2} \left|\widehat{h}_{j,f}\right|^2 - \sum\limits_{j=1}^{\lceil \sigma_\tau/T_\tau \rceil} \sum\limits_{f=-\lceil \sigma_v/2T_v \rceil}^{\lceil \sigma_v/2T_v \rceil} \left|\widehat{h}_{j,f}\right|^2}{\sum\limits_{j=1}^{M} \sum\limits_{f=-(D-1)/2}^{(D-1)/2} \left|\widehat{h}_{j,f}\right|^2}, & D \text{ is an odd number} \\[4ex] \dfrac{\sum\limits_{j=1}^{M} \sum\limits_{f=-D/2}^{D/2-1} \left|\widehat{h}_{j,f}\right|^2 - \sum\limits_{j=1}^{\lceil \sigma_\tau/T_\tau \rceil} \sum\limits_{f=-\lceil \sigma_v/2T_v \rceil}^{\lceil \sigma_v/2T_v \rceil} \left|\widehat{h}_{j,f}\right|^2}{\sum\limits_{j=1}^{M} \sum\limits_{f=-(D-1)/2}^{(D-1)/2} \left|\widehat{h}_{j,f}\right|^2}, & D \text{ is an even number} \end{cases} \tag{26}$$

By representing the enhanced channel matrix as $\overline{\mathbf{H}}_{\text{DD}} \in \mathbb{C}^{M \times D}$, its (j, f)-th element is determined by

$$\overline{h}_{j,f} = \begin{cases} \widehat{h}_{j,f}, & \left|\widehat{h}_{j,f}\right| \geq T_{\text{h,CE}} \\ 0, & \text{otherwise} \end{cases}, \tag{27}$$

where $\overline{h}_{j,f}$ denotes the (j, f)-th element of $\overline{\mathbf{H}}_{\text{DD}}$. In the absence of a LoS path, $\widetilde{T}_{\text{h}}$ (in Eq. (23)) is utilized as the detection threshold, thereby ensuring the applicability of the proposed method. Based on Eq. (22), the delay spread σ_τ and Doppler spread σ_v are leveraged as constraints on the channel response to further suppress estimation errors. By denoting the enhanced channel matrix of $\overline{\mathbf{H}}_{\text{DD}}$ as $\widetilde{\mathbf{H}}_{\text{DD}} \in \mathbb{C}^{M \times D}$, its (j, f)-th entry, i.e., $\widetilde{h}_{j,f}$, is given by

$$\widetilde{h}_{j,f} = \begin{cases} \overline{h}_{j,f}, & 1 \leq j \leq \left\lceil \frac{\sigma_\tau}{T_\tau} \right\rceil, |f| \leq \left\lceil \frac{\sigma_v}{2T_v} \right\rceil \\ 0, & \text{otherwise} \end{cases}. \tag{28}$$

Subsequently, the channel matrix $\widetilde{\mathbf{H}}_{\text{DD}}$ in the DD domain is transformed into the time-frequency domain by using the inverse symplectic finite Fourier transform (ISFFT) [43], yielding the enhanced time-frequency channel matrix $\widetilde{\mathbf{H}}_{\text{Eh}} \in \mathbb{C}^{M \times D}$, i.e.,

$$\widetilde{\mathbf{H}}_{\text{Eh}} = \mathbf{F}_M \widetilde{\mathbf{H}}_{\text{DD}} \mathbf{F}_D^H. \tag{29}$$

Thus, by leveraging the sensing-derived prior information constructed from both LoS and echo sensing, the proposed method significantly enhances the CE performance.

3.3. Sensing and Path-Sharing-aided Channel Reconstruction for SCCs

By setting the detection threshold $T_{\text{h,CE}}$, the channel path information of the PCC in the DD domain is achieved, and thus forms a reconstructed set of path delays and Doppler shifts $\mathcal{K}$ as

$$\mathcal{K} \triangleq \left\{ \tau_p, v_p \right\}_{p=1,2,\cdots,P}, \tag{30}$$

where τ_p and v_p denote the delay and Doppler shift of the p-th resolvable path, respectively. By leveraging the reconstructed set $\mathcal{K}$, a LoS-inspired CE scheme (based on path-sharing between PCC and SCCs) is proposed to reconstruct the channels of SCCs.

3.3.1. LoS path-based Reconstruction

In the presence of a LoS path, the transmission delays of the PCC and SCCs are approximately equal, i.e., $\widehat{\tau}_{\text{LoS,PCC}} = \widehat{\tau}_{\text{LoS,SCCs}}$. However, the different carrier frequencies of PCC and SCCs result in distinct Doppler shifts. Nevertheless, a proportional relationship exists between their respective carrier frequencies. By respectively denoting the frequencies of PCC and SCC as f_{PCC} and f_{SCC}, the corresponding Doppler indices are expressed as

$$
\begin{cases}
\nu_{\text{LoS}} = \dfrac{f_{d,p}}{T_{\nu,\text{PCC}}} = \dfrac{v_{\text{PCC}}f_{\text{PCC}}}{cT_{\nu,\text{PCC}}} \\[2mm]
\widehat{\nu}_{\text{LoS}} = \dfrac{f_{d,q}}{T_{\nu,\text{SCC}}} = \dfrac{v_{\text{SCC}}f_{\text{SCC}}}{cT_{\nu,\text{SCC}}}
\end{cases} ,
\tag{31}
$$

where $f_{d,p}$, v_{PCC}, and $T_{\nu,\text{PCC}}$ denote the Doppler shift of the LoS path, the velocity, and the Doppler resolution of the PCC, respectively. Accordingly, $f_{d,q}$, v_{SCC}, and $T_{\nu,\text{SCC}}$ represent the Doppler shift of the LoS path, the equivalent velocity, and the Doppler resolution for the SCC, respectively. Due to $v_{\text{PCC}} = v_{\text{SCC}}$, the Doppler index of the LoS path in the SCC satisfies

$$
\widehat{\nu}_{\text{LoS}} = \left\lceil \frac{\nu_{\text{LoS}} T_{\nu,\text{PCC}} f_{\text{SCC}}}{T_{\nu,\text{SCC}} f_{\text{PCC}}} \right\rceil .
\tag{32}
$$

Based on Eq. (32), the Doppler index corresponding to the channel response of the SCC in the DD domain is obtained. However, this shared property does not extend to the complex gain of the channel, i.e., the amplitude and phase of the channel response. Therefore, further estimation of the complex channel gain is required to reconstruct the SCC channel.

To reduce the pilot overhead for the SCC and leverage the channel path-sharing property, a small number of pilot symbols are employed to estimate the complex channel gain. In this paper, the first OFDM symbol in the received frame of the SCC is utilized as the pilot symbol for complex channel gain estimation. By denoting the estimated CFR vector as $\widehat{\mathbf{H}}_{\text{SCC}} \in \mathbb{C}^{M\times 1}$, its m-th entry, i.e., $\widehat{H}_{\text{SCC}}(m)$, is given by

$$
\widehat{H}_{\text{SCC}}(m) = \frac{y_{\text{SCC}}(m)}{p_{\text{SCC}}(m)},
\tag{33}
$$

where $y_{\text{SCC}}(m)$ and $p_{\text{SCC}}(m)$ denote the m-th entries of the received pilot vector $\mathbf{y}_{\text{SCC}} \in \mathbb{C}^{M\times 1}$ and the transmitted pilot vector $\mathbf{p}_{\text{SCC}} \in \mathbb{C}^{M\times 1}$ for the SCC, respectively. By applying the IDFT, the CFR matrix is transformed into the time domain, yielding

$$
\widehat{\mathbf{h}}_{\text{SCC}} = \mathbf{F}_M \widehat{\mathbf{H}}_{\text{SCC}},
\tag{34}
$$

where $\widehat{\mathbf{h}}_{\text{SCC}} \in \mathbb{C}^{M\times 1}$ represents the estimated CIR matrix of the SCC. In this paper, the time-domain channel gain $\widehat{\mathbf{h}}_{\text{SCC}}(m)$ is utilized to approximate the complex channel gain at the corresponding delay in the DD domain. By representing the channel matrix of the SCC in the DD domain as $\widehat{\mathbf{H}}_{\text{DD,SCC}} \in \mathbb{C}^{M\times D}$, the channel response corresponding to the index $(\widehat{\tau}_{\text{LoS,SCC}}, \widehat{\nu}_{\text{LoS}})$ of the LoS path of the SCC in the DD domain, denoted as $\widehat{h}_{\text{DD,SCC}}^{\widehat{\tau}_{\text{LoS,SCC}}, \widehat{\nu}_{\text{LoS}}}$, is given by

$$
\widehat{h}_{\text{DD,SCC}}^{\widehat{\tau}_{\text{LoS,SCC}}, \widehat{\nu}_{\text{LoS}}} = \widehat{h}_{\text{SCC}}(\widehat{\tau}_{\text{LoS,SCC}}),
\tag{35}
$$

where $\widehat{h}_{\text{SCC}}(\widehat{\tau}_{\text{LoS,SCC}})$ denotes the channel response of the LoS path of $\widehat{\mathbf{h}}_{\text{SCC}}$.

3.3.2. NLoS path-based Reconstruction

Building upon the LoS path-sharing mechanism, we further extend this path-sharing framework to NLoS scenarios. For clarity, the path delay sets of the PCC and the SCC are defined as $\mathcal{A} \triangleq \left\{ \tau_p \right\}_{p=1,\cdots,P}$

and $\mathcal{B} \triangleq \{\widehat{\tau}_m\}_{m=1,\cdots,M}$, respectively. For the case where the path delay of the PCC coincides with that of the SCC, the intersection set is given by

$$\mathcal{A} \cap \mathcal{B} = \{\widehat{\tau}_g, g = 1, 2, \cdots, G\}, \tag{36}$$

where $\widehat{\tau}_g$ denotes the g-th shared path with identical delay between the PCC and SCC. By leveraging the proportional relationship between the carrier frequencies of the shared paths, the channel parameters of the SCC in the Doppler direction are reconstructed. According to Eq. (32), the Doppler index of the g-th path in the SCC is given by

$$\widehat{\nu}_g = \left\lceil \frac{\nu_g T_{\nu,\text{PCC}} f_{\text{SCC}}}{T_{\nu,\text{SCC}} f_{\text{PCC}}} \right\rceil. \tag{37}$$

Subsequently, the channel response corresponding to the index of the g-th path (i.e., $(\widehat{\tau}_g, \widehat{\nu}_g)$) in the DD domain for the SCC, denoted as $\widehat{h}_{\text{DD,SCC}}^{\widehat{\tau}_g, \widehat{\nu}_g}$, is given by

$$\widehat{h}_{\text{DD,SCC}}^{\widehat{\tau}_g, \widehat{\nu}_g} = \widehat{h}_{\text{SCC}}(\widehat{\tau}_g), \tag{38}$$

where $\widehat{h}_{\text{SCC}}(\widehat{\tau}_g)$ denotes the channel response of the g-th path of $\widehat{\mathbf{h}}_{\text{SCC}}$. By combining Eq. (35) and Eq. (38), the (j, f)-th element of the reconstructed channel matrix $\widehat{\mathbf{H}}_{\text{DD,SCC}} \in \mathbb{C}^{M \times D}$ of the SCC, denoted as $\widehat{h}_{\text{DD,SCC}}^{j,f}$, is rewritten as

$$\begin{cases} \widehat{h}_{\text{DD,SCC}}^{\tau_{\text{LoS,SCC}}, \widehat{\nu}_{\text{LoS}}} = \widehat{h}_{\text{SCC}}(\widehat{\tau}_{\text{LoS,SCC}}), \widehat{\tau}_{\text{LoS,PCC}} = \widehat{\tau}_{\text{LoS,SCC}} \\ \widehat{h}_{\text{DD,SCC}}^{\widehat{\tau}_g, \widehat{\nu}_g} = \widetilde{h}_{\text{SCC}}(\widehat{\tau}_g), \widehat{\tau}_g \in (\mathcal{A} \cap \mathcal{B}) \\ \widehat{h}_{\text{DD,SCC}}^{j,f} = 0, \text{others} \end{cases}. \tag{39}$$

Thus, an initial reconstruction of the SCC channel is performed by leveraging the channel path-sharing mechanism. However, the channel paths are not fully shared between the PCC and SCCs, limiting the accuracy of the channel reconstruction. To address this, an iterative processing scheme is employed to reconstruct the non-shared channel paths while mitigating the reconstruction errors.

3.3.3. Iterative Channel Reconstruction and Enhancement for SCCs

With the reconstructed channel $\widehat{\mathbf{H}}_{\text{DD,SCC}}$ (according to Eq. (39)), it is transformed into the time-frequency domain by using the ISFFT. By denoting the transformed version as $\mathbf{H}_{\text{SCC}} \in \mathbb{C}^{M \times D}$, we have

$$\mathbf{H}_{\text{SCC}} = \mathbf{F}_M \widehat{\mathbf{H}}_{\text{DD,SCC}} \mathbf{F}_D^H. \tag{40}$$

By denoting the received signal of the SCC as $\mathbf{Y}_{\text{SCC}} \in \mathbb{C}^{M \times D}$, the received signal at data positions (denoted as $\mathbf{Y}_{\text{SCC,data}} \in \mathbb{C}^{M \times (D-1)}$) and the channel matrix (i.e., $\mathbf{H}_{\text{SCC,data}} \in \mathbb{C}^{M \times (D-1)}$) are extracted to perform zero-forcing (ZF) equalization. The (m, d)-th element of the equalized data $\widehat{\mathbf{X}}_{\text{SCC,data}} \in \mathbb{C}^{M \times (D-1)}$, denoted as $\widehat{X}_{\text{SCC,data}}(m, d)$, is given by

$$\widehat{X}_{\text{SCC,data}}(m, d) = \frac{Y_{\text{SCC,data}}(m, d)}{H_{\text{SCC,data}}(m, d)}, \tag{41}$$

where $Y_{\text{SCC,data}}(m, d)$ and $H_{\text{SCC,data}}(m, d)$ denote the (m, d)-th elements of $\mathbf{Y}_{\text{SCC,data}} \in \mathbb{C}^{M \times (D-1)}$ and $\mathbf{H}_{\text{SCC,data}} \in \mathbb{C}^{M \times (D-1)}$, respectively. Subsequently, data $\widehat{\mathbf{X}}_{\text{SCC,data}}$ is demodulated and then remodulated to obtain $\mathbf{X}_{\text{SCC,data}} \in \mathbb{C}^{M \times (D-1)}$. The signal $\mathbf{X}_{\text{SCC,data}}$ and the pilot signal $\mathbf{p}_{\text{SCC}}$ are concatenated to form the complete time-frequency signal $\mathbf{X}_{\text{SCC}} \in \mathbb{C}^{M \times D}$, i.e.,

$$\mathbf{X}_{\text{SCC}} = [\mathbf{p}_{\text{SCC}}, \mathbf{X}_{\text{SCC,data}}]. \tag{42}$$

Subsequently, $\mathbf{X}_{\text{SCC}}$ is utilized as the pilot signal, and the CE for the SCC is performed according to Eq. (16), thereby obtaining $\widehat{\mathbf{H}}_{\text{SCC}} \in \mathbb{C}^{M \times N}$. Furthermore, the estimated $\widehat{\mathbf{H}}_{\text{SCC}}$ is enhanced using Eq. (19) to Eq. (29). By leveraging prior information assisted by LoS and echo sensing, the reconstruction errors introduced during the reconstruction stage are mitigated, thereby yielding the enhanced channel matrix $\widehat{\mathbf{H}}_{\text{TF,SCC}}$ for the SCC.

Since the reconstruction errors introduced during the reconstruction stage cannot be eliminated in a single iteration, the operations from Eq. (19) to Eq. (29) are iteratively applied to enhance the CE accuracy of the SCC, ultimately yielding the enhanced channel matrix $\widetilde{\mathbf{H}}_{\text{TF,SCC}}$ for the SCC.

4. Simulation Results and Analysis

In this section, numerical simulations are conducted to validate the effectiveness and robustness of the proposed LoS and echo sensing-assisted CE method in UAV communication scenarios. The simulation parameters and methodology are presented in Section 4.1. In Section 4.2, the computational complexity of the proposed scheme and baseline methods is analyzed. The effectiveness of the proposed method and its robustness against parameter variations are evaluated in Section 4.3 and Section 4.4, respectively.

4.1. Parameter Settings

The basic simulation parameters involved are given as follows. For the communication system, the number of CCs is set to $B = 2$, with carrier frequencies of the PCC and SCC being 2.4 GHz and 5.8 GHz, respectively. The duration of each time slot is 1 ms. The number of subcarriers and OFDM symbols per slot are set to $M = 72$ and $D = 14$, respectively, with a subcarrier spacing of $\Delta f_{\text{Com}} = 15$ kHz and a CP length of $L_{\text{CP}} = M/4$. The PCC employs a comb-type pilot structure with a pilot interval of 2. The false alarm probabilities for the path threshold and the LoS-based threshold are set to $P_{\text{fa}} = 10^{-8}$ and $P_{\text{fL}} = 10^{-3}$, respectively. The bit stream is modulated by the quadrature phase shift keying (QPSK) mode. For the echo sensing system, an OFDM radar system with a carrier frequency of $f_c = 2.1$ GHz is considered. The number of subcarriers is $S = 1024$, the number of OFDM symbols is $K = 256$, the subcarrier spacing is $\Delta f = 111.25$ kHz, the OFDM symbol duration is $T_c = 2.25$ μs, and the total symbol duration (including CP) is $T_d = 11.25$ μs. According to [31], the false alarm probability of the 2D CA-CFAR detector is set to $P_f = 10^{-6}$, and the number of reference cells is set to $N_g = 28$. The power delay profile (PDP) of the channel model adopts the TDL-D channel model, and the Rician factor $\mathcal{K}$ is randomly generated within the interval $[3, 13]$. To simulate the existence of non-shared paths between the channels of PCC and SCC, their path-number difference, denoted as Δ_L, is randomly chosen as $\Delta_L = 0$ or $\Delta_L = 1$. The UAV velocity and distance are set to $v = 25$ m/s and $d = 500$ m, respectively. By respectively representing the received signal power and the noise variance as P_r and σ_n^2, the signal-to-noise ratio (SNR) in decibels (dB) is defined as SNR $= 10\log_{10}(P_r/\sigma_n^2)$, and the normalized mean square error (NMSE) is defined as

$$\text{NMSE} = \mathbb{E}\left\{ \frac{\left\| \widetilde{\mathbf{H}} - \mathbf{H} \right\|_2^2}{\|\mathbf{H}\|_2^2} \right\}, \tag{43}$$

where $\widetilde{\mathbf{H}}$ is the estimate of the true channel $\mathbf{H}$. To evaluate the effectiveness of the proposed method, the following schemes are adopted in the subsequent simulation analysis:

- LS: Classic least squares with linear interpolation;
- DFT_based: LS with DFT enhancement;
- OMP_based: Classic CS-based CE scheme;
- LoS_based: LoS sensing-based CE enhancement scheme in [16];
- LS_DD: LS enhancement with sensing-aided scheme in DD domain in [31];
- Path_gains_based: Path gain-based CE enhancement scheme in [32];
- Prop_PCC: Proposed CE enhancement scheme for PCC;

- Prop_SCC: Proposed channel reconstruction scheme for SCC;
- Prop_iter: Proposed iterative Channel Reconstruction and Enhancement for SCC;

where "LS", "DFT_based", "OMP_based", "LoS_based", "LS_DD", and "Path_gains_based" are employed as baseline schemes.

4.2. Computational Complexity Analysis

The complex multiplication (CM) is employed to evaluate the computational complexity of both the proposed and comparative methods. For "LS", the CMs are primarily caused by CE at pilot positions and interpolation operation at data positions. Due to the pilot interval of 2, the CMs of "LS" at pilot positions are $MD/2$. To obtain the channel at data positions, linear interpolation is applied to recover the complete CFR, requiring additional CMs of $MD/2$. Thus, the total CMs of the "LS" are MD. For "DFT_based", "Path_gains_based", and "LoS_based", additional transform-domain operations are required relative to "LS". This consumes one IDFT and one DFT operation along the subcarrier direction for D symbols, resulting in $2M^2D$ CMs. Although time-domain filtering or thresholding operations are employed to perform denoising, we ignore these CMs for "DFT_based", "Path_gains_based", and "LoS_based" due to their insignificance. Hence, the total CMs for these methods remain approximately $2M^2D$. For the CS-based "OMP_based" method, each symbol entails an iterative processing with a sparsity of K, yielding the CMs of M^2DK. Additionally, a DFT operation along the subcarrier direction is required to transform the CIR to the frequency domain, with the corresponding CMs of M^2D. Thus, the total CMs of "OMP_based" are $M^2DK + M^2D$. For "LS_DD", the CMs are divided into sensing and communication parts. The sensing part primarily includes a 2D-DFT and a 2D CA-CFAR detection, requiring the CMs of $M^2D + MD^2$. For CE enhancement processing, the operation involves one IDFT and one DFT, each with additional $M^2D + MD^2$ CMs relative to "LS". In total, the CMs for "LS_DD" are $2MD + 3M^2D + 3MD^2$.

For the proposed method "Prop_PCC", the CMs for CE are MD. Compared to "LS_DD", "Prop_PCC" introduces additional sensing operations and LoS-based threshold refinement. Nonetheless, these operations primarily involve additive and subtractive calculations. Hence, the total CMs required for "Prop_PCC" are approximately $2MD + 3M^2D + 3MD^2$. For the SCC, the CMs required for complex channel gain estimation are M. In addition, one transform-domain operation involving an IDFT and a DFT is needed, with the CMs being $M^2D + MD^2$. Hence, the total CMs for the "Prop_SCC" are $M + M^2D + MD^2$. To improve reconstruction accuracy of SCC, the CMs for one iteration of the SCC channel enhancement are $4MD + 2M^2D + 2MD^2$. With N_{iter} iterations, the total CMs of "Prop_iter" are $M + M^2D + MD^2 + N_{\text{iter}}(4MD + 2M^2D + 2MD^2)$.

4.3. Effectiveness Analysis

To analyze the effectiveness of the proposed method, Figure 1 and Figure 2 present the NMSE and bit error rate (BER) performance for the PCC, respectively. From Figure 1, for each given SNR, the NMSEs of "DFT_based", "Path_gains_based", and "LoS_based" are lower than that of "LS". For the case where SNR = 10 dB, the NMSE of "LS" is 3.90×10^{-2}, while the NMSEs of "DFT_based", "Path_gains_based", and "LoS_based" are 2.33×10^{-2}, 2.11×10^{-2}, and 1.76×10^{-2}, respectively.
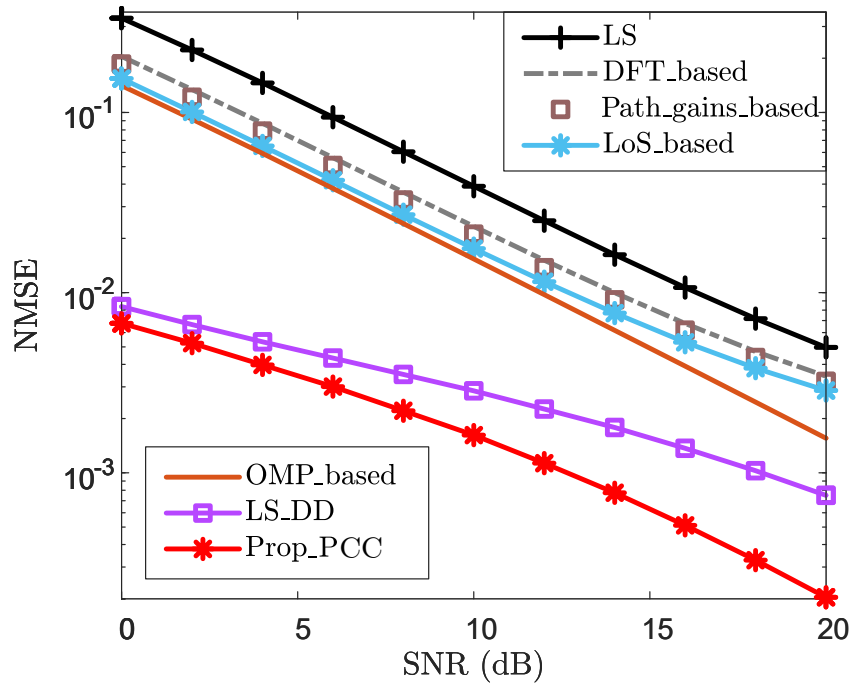
Figure 1. NMSE vs. SNR for PCC.

Furthermore, "LoS_based" outperforms both "DFT_based" and "Path_gains_based" for each specific SNR in terms of NMSE, demonstrating the effectiveness and superiority of leveraging LoS sensing to enhance CE accuracy. For CS-based method "OMP_based", it effectively improves NMSE performance by utilizing sparse reconstruction. However, this method requires precise knowledge of the sparsity, which hinders its practical applications. By leveraging echo sensing-aided prior information, "LS_DD" and "Prop_PCC" achieve significantly superior NMSE performance compared to "LS", "DFT_based", "Path_gains_based", "LoS_based", and "OMP_based". When SNR = 12 dB, the NMSEs of "LS_DD" and "Prop_PCC" are 2.26×10^{-3} and 1.13×10^{-3}, respectively, while the NMSEs of "LS", "DFT_based", "Path_gains_based", "LoS_based", and "OMP_based" all exceed 9.75×10^{-3}. This demonstrates that leveraging echo sensing-aided prior information significantly enhances CE accuracy. Furthermore, "Prop_PCC" consistently outperforms "LS_DD" in terms of NMSE performance for each given SNR. This improvement is attributed to the fact that "Prop_PCC" incorporates LoS sensing-based prior information to design an effective path detection threshold, thereby further refining CE accuracy.
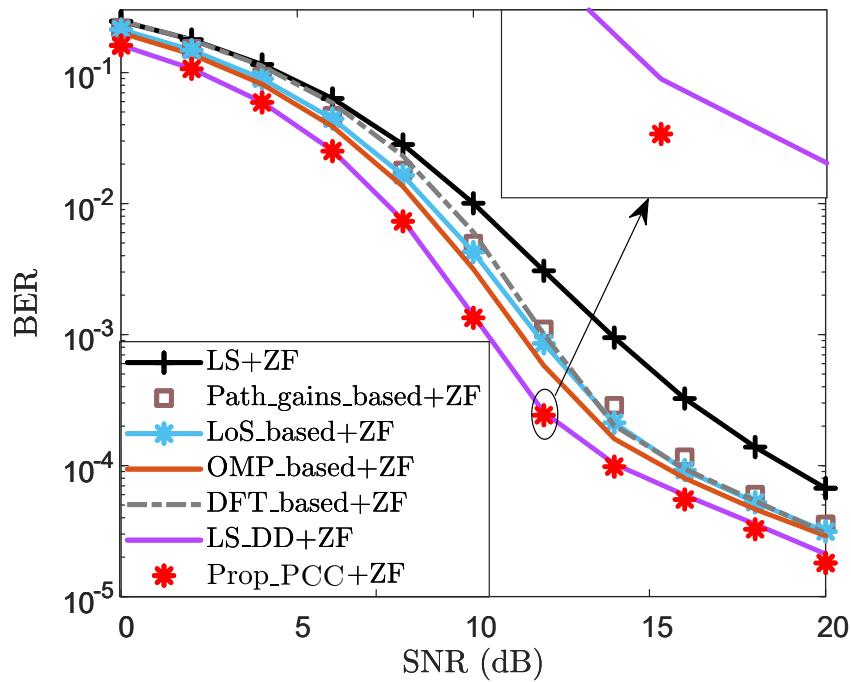
Figure 2. BER vs. SNR for PCC.

To further validate BER effectiveness of the proposed method, Figure 2 depicts the BER performance curves. For each given SNR, "LoS_based+ZF" achieves superior BER performance compared to "LS+ZF", "LS_DFT+ZF", and "Path_gains_based+ZF". When SNR = 12 dB, the BER of "LoS_based+ZF" is 4.26×10^{-3}, while those of "LS+ZF", "LS_DFT+ZF", and "Path_gains_based+ZF" all exceed 4.95×10^{-3}. This result demonstrates that LoS sensing is effective in reducing the BER. The primary reason is that the utilization of LoS sensing-based prior information mitigates CE errors, thereby improving the BER performance. In Figure 2, the BER performance of both "LS_DD+ZF" and "Prop_PCC+ZF" is lower than that of "LS+ZF", "LS_DFT+ZF", "Path_gains_based+ZF", "LoS_based+ZF", and "OMP_based+ZF" for each given SNR. This indicates that "LS_DD+ZF" and "Prop_PCC+ZF" enhance the CE accuracy by leveraging echo sensing-based information, and thus refine their BER performance. Furthermore, "Prop_PCC+ZF" achieves slightly superior BER performance compared to "LS_DD+ZF" for each specific SNR. For the case where SNR = 12dB, the BER of "Prop_PCC+ZF" is 2.42×10^{-4}, whereas that of "LS_DD+ZF" is 2.55×10^{-4}. This result demonstrates that the proposed method effectively integrates both LoS sensing and echo sensing information, thereby enhancing the CE performance. Consequently, "Prop_PCC+ZF" exhibits a discernible advantage in terms of BER performance.

To evaluate the effectiveness of the SCC channel reconstruction, Figure 3 and Figure 4 present the NMSE and BER performance, respectively. To ensure a fair comparison in terms of NMSE performance, the same pilot-assisted CE scheme as used for the PCC is adopted as the baseline. Notably, the proposed scheme requires only 72 pilots, with a total number of resource elements amounting to 1008. In contrast, the baseline method utilizes 504 pilots, which is approximately seven times that of the proposed scheme. When SNR $\geq$ 10dB, "Prop_SCC" achieves superior NMSE performance compared to the "LS+ZF", "LS_DFT+ZF", "Path_gains_based+ZF", and "LoS_based+ZF". This demonstrates that in relatively high SNR region, "Prop_SCC" not only reduces pilot overhead but also enhances channel reconstruction performance relative to the baseline methods.
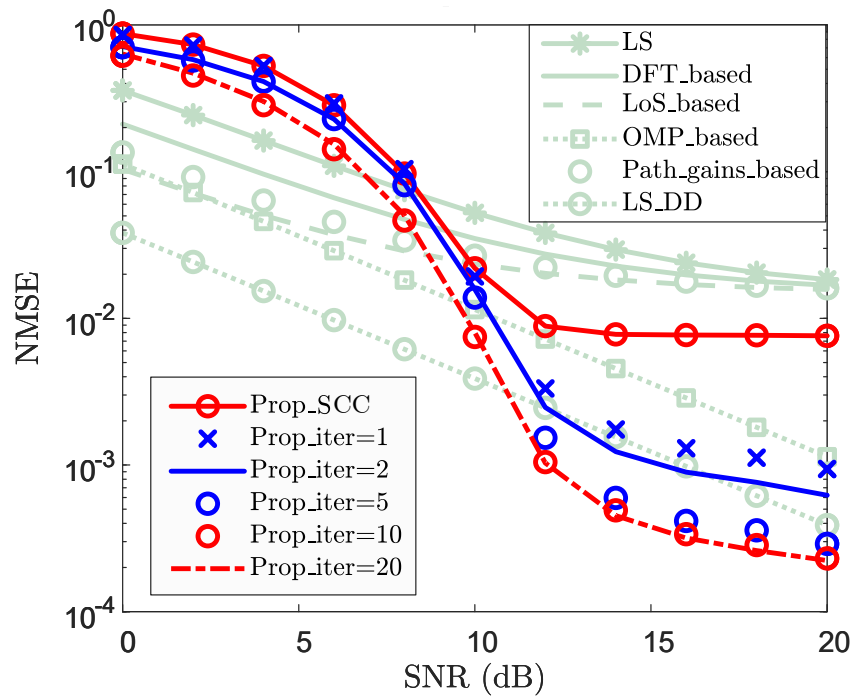
Figure 3. NMSE vs. SNR for SCC.

However, for the case where SNR $\geq$ 10dB, "OMP_based" and "LS_DD" achieve smaller NMSEs than that of "Prop_SCC". Nevertheless, "Prop_SCC" does not require an accurate sparsity as a prior information compared to "OMP_based", and exhibits a lower computational complexity even compared to "LS_DD". When SNR = 12dB, the NMSEs of "Prop_SCC", "Prop_iter=1", "Prop_iter=2", "Prop_iter=10", "Prop_iter=15", and "Prop_iter=20" are 8.86×10^{-3}, 3.33×10^{-3}, 2.47×10^{-3}, 1.53×10^{-3}, 1.05×10^{-3}, and 1.03×10^{-3}, respectively. This demonstrates that the NMSEs of the SCC channel reconstruction are improved as the number of iterations increases. When the number of iterations exceeds 10 and SNR $\geq$ 10dB, "Prop_iter=15" and "Prop_iter=20" achieve better NMSE performance than "LS_DD". This indicates that iterative processing significantly enhances the NMSE performance of the proposed scheme with increased computational complexity. Nonetheless, the pilot overhead of the proposed method remains substantially lower than that of the baseline schemes. Overall, the proposed approach achieves effective reconstruction accuracy with considerably reduced pilot overhead.
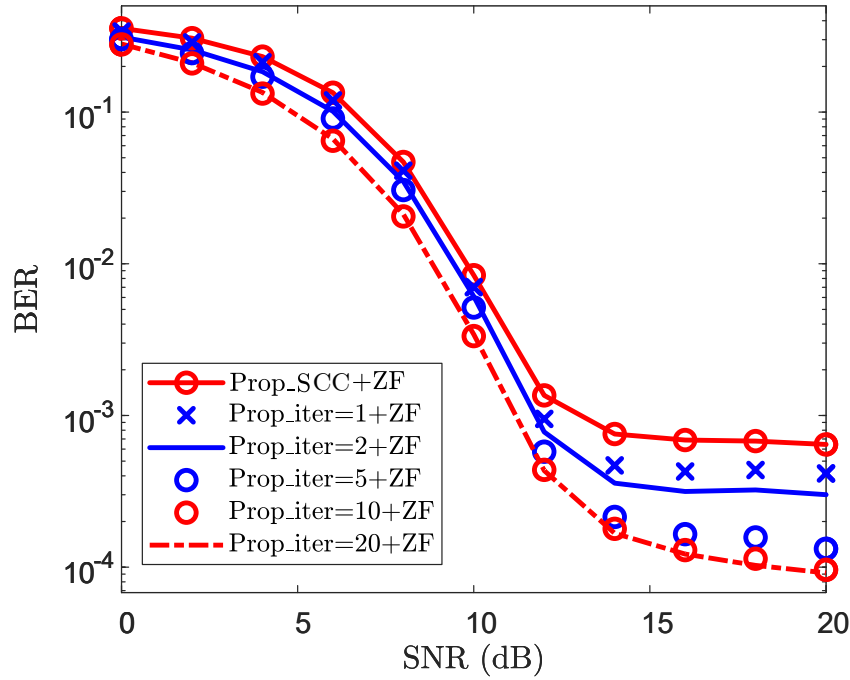
Figure 4. BER vs. SNR for SCC.

Figure 4 presents the BER performance of the SCC channel reconstruction. From Figure 4, the BER performance improves as the number of iterations increases, and this trend becomes more pronounced in relatively high SNR region (e.g., SNR $\geq$ 12dB). For the case where SNR = 8dB, the BERs of "Prop_SCC+ZF", "Prop_iter=1+ZF", "Prop_iter=2+ZF", "Prop_iter=10+ZF", "Prop_iter=15+ZF", and "Prop_iter=20+ZF" are 4.69×10^{-2}, 4.11×10^{-2}, 3.49×10^{-2}, 3.06×10^{-2}, 2.12×10^{-2}, and 2.05×10^{-2}, respectively. In contrast, when SNR = 16dB, the BERs of "Prop_SCC+ZF", "Prop_iter=1+ZF", "Prop_iter=2+ZF", "Prop_iter=10+ZF", "Prop_iter=15+ZF", and "Prop_iter=20+ZF" are reduced to 6.89×10^{-4}, 4.27×10^{-4}, 3.15×10^{-4}, 1.65×10^{-4}, 1.29×10^{-4}, and 1.22×10^{-4}, respectively. Furthermore, the proposed method has 936 resource elements per time slot for symbol transmission, whereas the baseline methods only have 504. With the QPSK modulation, the proposed method transmits 1872 bits per time slot, while only 1008 bits being transmitted by the baseline methods. Under the same conditions, the proposed scheme achieves approximately 1.85 times the data transmission volume of the baseline methods. Thus, by leveraging sensing information and path-sharing to reconstruct the SCC channel, the proposed method reduces the pilot overhead of the SCC and thereby increases the data transmission rate.

4.4. Robustness Analysis

To verify the robustness of the proposed method, this section evaluates the impact of velocity v, the path-number difference Δ_L, and the carrier frequency of the SCC, respectively. Except for the parameters discussed in this section, all other fundamental parameters remain consistent with those detailed in Section 4.1.

4.4.1. Robustness Against Velocity v

In wireless communication systems, different velocities may affect the CE accuracy. To validate the robustness of the proposed method against velocity variations, Figure 5 and Figure 6 demonstrate the NMSE performance of the PCC and SCC against the impact of the variations of velocity, where $v = 20\text{m/s}$, $v = 25\text{m/s}$, and $v = 30\text{m/s}$ are considered.
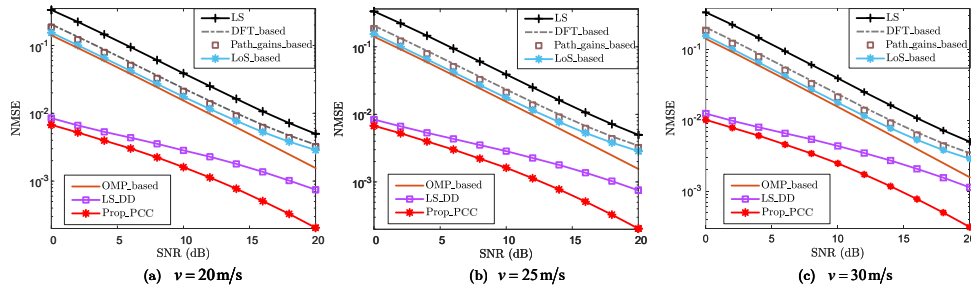
Figure 5. NMSE vs. SNR for PCC against velocity v, where $v = 20$ m/s, $v = 25$ m/s, and $v = 30$ m/s are considered.

From Figure 5, the proposed method, i.e., "Prop_PCC" achieves a significantly lower NMSE than "LS", "DFT_based", "Path_gains_based", "LoS_based", "OMP_based", and "LS_DD" for each given SNR and velocity. For the case where $v = 30$m/s and SNR = 16dB, the NMSEs of "LS", "DFT_based", "Path_gains_based", and "LoS_based", "OMP_based", and "LS_DD" are 1.07×10^{-2}, 6.75×10^{-3}, 6.19×10^{-3}, 5.29×10^{-3}, 3.93×10^{-3}, and 2.06×10^{-3}, respectively, while the NMSE of "Prop_PCC" is only 7.71×10^{-4}. This demonstrates that the proposed method significantly enhances CE accuracy by effectively leveraging both LoS and echo sensing information. As the velocity increases from $v = 20$m/s to $v = 30$m/s, the Doppler shift also rises proportionally. As depicted in Figure 5, the NMSE performance remains consistent as the velocity increases. The primary reason is that, for all given velocity, the channel coherence time remains sufficiently longer than the time slot duration. According to the definition of channel coherence time, i.e., $T_{ct} \approx 0.423/f_{D,max}$, when the velocities are $v = 20$m/s, $v = 25$m/s, and $v = 30$m/s, the coherence times of the PCC channel are approximately 3 ms, 2.4 ms, and 2 ms, respectively. Consequently, the proposed method effectively enhances NMSE performance regardless of the variation in velocity.
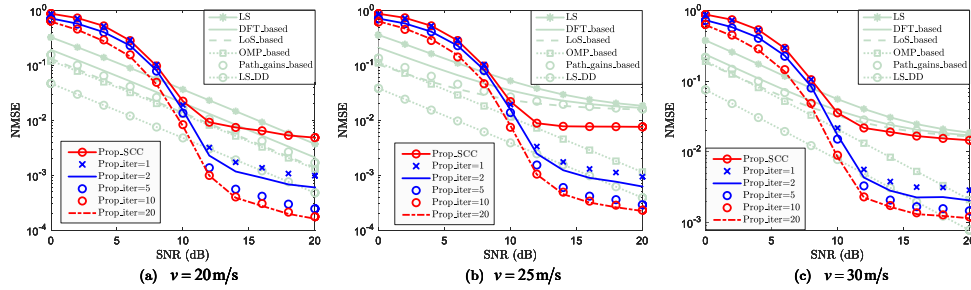

Figure 6. NMSE vs. SNR for SCC against velocity v, where $v = 20$ m/s, $v = 25$ m/s, and $v = 30$ m/s are considered.

In Figure 6, the NMSE performance of the SCC channel reconstruction with varying velocity is demonstrated. For the case where SNR = 14dB, the NMSEs of "Prop_iter=15" for the velocities $v = 20$m/s, $v = 25$m/s, and $v = 30$m/s are 3.88×10^{-4}, 4.52×10^{-4}, and 1.66×10^{-3}, respectively. Correspondingly, the approximate channel coherence times of the SCC are 1.6 ms, 1.3 ms, and 1.1 ms for the velocities of $v = 20$m/s, $v = 25$m/s, and $v = 30$m/s, respectively. The NMSE performance of the SCC channel reconstruction deteriorates as the velocity increases due to the increased Doppler shift interference. Nevertheless, the reconstruction performance of the SCC achieves NMSE performance comparable to that of the baseline methods for each given velocity and SNR, especially in relatively high SNR region (e.g., SNR ≥ 10dB). Especially, the proposed method requires significantly lower pilot overhead compared to the baseline methods, making it highly attractive for reconstructing the SCC channels.

4.4.2. Robustness Against Path-number Difference Δ_L

To evaluate the impact of Δ_L, the NMSE performance of the SCC reconstruction is validated, where the cases of $\Delta_L = [0, 1]$, $\Delta_L = [0, 3]$, and $\Delta_L = [0, 5]$ are considered. As shown in Figure 7,

the NMSE performance of the SCC reconstruction degrades as Δ_L increases. This is primarily due to the introduction of additional unreconstructed path errors in the SCC channel beyond the path-sharing reconstruction stage. Although such errors are partially mitigated by increasing the number of iterations, they still lead to a degradation in reconstruction performance. As Δ_L increases, the presence of LoS sensing jointly mitigates this performance loss.
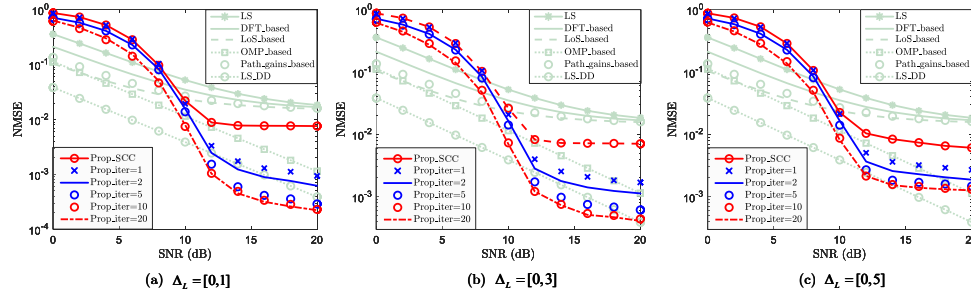

Figure 7. NMSE vs. SNR for SCC against path-number difference Δ_L, where $\Delta_L = [0,1]$, $\Delta_L = [0,3]$, and $\Delta_L = [0,5]$ are considered.

4.4.3. Robustness Against Carrier Frequency of SCC

CA systems typically operate with multiple SCC frequency bands. To validate the effectiveness of SCC reconstruction against the impact of carrier frequency, Figure 8 plots the NMSE performance, where 4 GHz, 5.8 GHz, and 7.9 GHz are considered for the SCC bands. From Figure 8, the proposed method effectively reconstructs the SCC channel across all evaluated frequency bands. Furthermore, the reconstruction performance improves as the number of iterations increases. However, the reconstruction accuracy slightly degrades as the carrier frequency of the SCC increases. The primary reason for this is that a higher carrier frequency results in an increase of Doppler shift for the paths, which amplifies the reconstruction error introduced by non-shared paths and consequently degrades the overall reconstruction performance. Furthermore, as the Doppler shift increases, the channel correlation is weakened correspondingly. When the carrier frequencies are 4 GHz, 5.8 GHz, and 7.9 GHz, the channel coherence times of the SCC are approximately 1.3 ms, 0.875 ms, and 0.642 ms, respectively. As the first symbol is utilized for path gain reconstruction, the increase of carrier frequency thereby increases its reconstruction errors due to larger Doppler shifts and reduced coherence time. Despite the performance degradation caused by increasing velocity, the proposed method still effectively reconstructs the SCC channel with low pilot overhead. From a resource efficiency perspective, the proposed approach presents a highly attractive solution for channel reconstruction in CA systems.
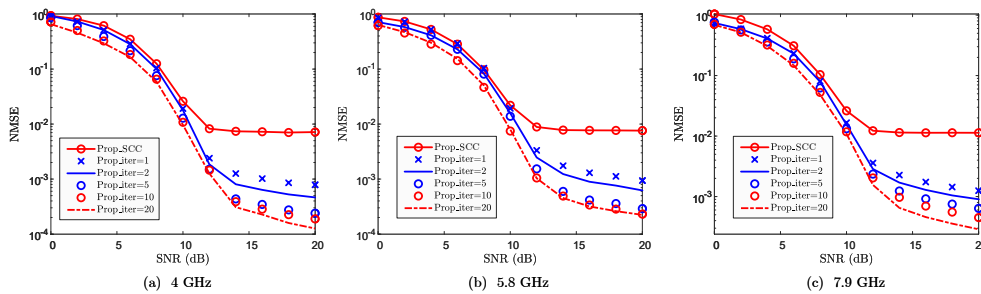

Figure 8. NMSE vs. SNR against carrier frequency of SCC, where 4 GHz, 5.8 GHz, and 7.9 GHz are considered.

5. Conclusions

In this paper, we investigate CE in UAV-assisted OFDM systems by leveraging LoS and echo sensing with CA. By exploiting the prominent LoS characteristics and echo sensing information in UAV communication scenarios, sensing-assisted prior information is established. Based on this prior information, the CE accuracy of the PCC in CA is significantly improved. Inspired by the LoS path, a method for reconstructing the SCCs channel is proposed by exploiting the path-sharing property

between the PCC and SCCs. Furthermore, this path sharing is extended to NLoS paths for enhancing the reconstruction of the SCCs channel. By leveraging the path-sharing property between the PCC and SCCs, the pilot overhead of the SCCs is significantly reduced. To reconstruct non-shared paths and mitigate reconstruction errors, an iterative processing scheme is developed. This scheme enhances the accuracy of the SCCs channel reconstruction. Simulation results demonstrate the effectiveness of the proposed method in enhancing the CE accuracy for both PCC and SCCs. Against parameter variations, the proposed method also exhibits its robustness.

References

1. Y. Jiang, X. Li, G. Zhu, H. Li, J. Deng, K. Han, C. Shen, Q. Shi, and R. Zhang, "Integrated Sensing and Communication for Low Altitude Economy: Opportunities and Challenges," *IEEE Commun. Mag.*, pp. 1–7, early access, 2025.
2. K. He, Q. Zhou, Z. Lian, Y. Shen, J. Gao, and Z. Shuai, "Spatiotemporal Precise Routing Strategy for Multi-UAV-Based Power Line Inspection With Integrated Satellite-Terrestrial Network," *IEEE Trans. Ind. Appl.*, vol. 60, no. 6, pp. 8418–8429, Dec. 2024.
3. S. Meng, S. Wu, J. Zhang, J. Cheng, H. Zhou, and Q. Zhang, "Semantics-Empowered Space-Air-Ground-Sea Integrated Network: New Paradigm, Frameworks, and Challenges," *IEEE Commun. Surveys Tuts.*, vol. 27, no. 1, pp. 140–183, Feb. 2025.
4. G. Geraci, A. Garcia-Rodriguez, M. M. Azari, A. Lozano, M. Mezzavilla, S. Chatzinotas, Y. Chen, S. Rangan, and M. D. Renzo, "What Will the Future of UAV Cellular Communications Be? A Flight From 5G to 6G," *IEEE Commun. Surveys Tuts.*, vol. 24, no. 3, pp. 1304–1335, 3rd Quart., 2022.
5. S. Kumari, K. K. Srinivas, and P. Kumar, "Channel and Carrier Frequency Offset Equalization for OFDM Based UAV Communications Using Deep Learning," *IEEE Commun. Lett.*, vol. 25, no. 3, pp. 850–853, Mar. 2021.
6. H. Lin, Z. Zhang, X. Pan, X. Luo, and Y. Cheng, "Joint Channel Estimation and Symbol Detection for UAV-Assisted Systems Using Tensor Framework," in *Proc. IEEE 22nd Int. Conf. Commun. Technol. (ICCT)*, Nanjing, China, Nov. 2022, pp. 1025–1030.
7. S. Chen, C. Liu, and L. Huang, "Estimation of Pilot-assisted OFDM Channel Based on Multi-Resolution Deep Neural Networks," in *Proc. IEEE Int. Conf. Unmanned Syst. (ICUS)*, Guangzhou, China, Oct. 2022, pp. 764–769.
8. B. He, X. Ji, G. Li, and B. Cheng, "Key Technologies and Applications of UAVs in Underground Space: A Review," *IEEE Trans. Cognit. Commun. Netw.*, vol. 10, no. 3, pp. 1026–1049, Jun. 2024.
9. M.-S. Kim, "Single-Input Multiple-Output (SIMO) Cascode Low-Noise Amplifier with Switchable Degeneration Inductor for Carrier Aggregation," *Sensors*, vol. 24, no. 20, p. 6606, Oct. 2024.
10. 3rd Generation Partnership Project (3GPP), "Feasibility study for further enhancements for E-UTRA (LTE Advanced)," 3GPP, Sophia Antipolis, France, Tech. Rep. 36.912 version 9.1.0 Release 9, Sep. 2009.
11. G. Yuan, X. Zhang, W. Wang, and Y. Yang, "Carrier aggregation for LTE-advanced mobile communication systems," *IEEE Commun. Mag.*, vol. 48, no. 2, pp. 88–93, Feb. 2010.
12. H. Liu, Z. Wei, J. Piao, H. Wu, X. Li, and Z. Feng, "Carrier Aggregation Enabled MIMO-OFDM Integrated Sensing and Communication," *IEEE Trans. Wireless Commun.*, vol. 24, no. 6, pp. 4532–4548, Jun. 2025.

13. W. Lu, P. Si, Y. Gao, H. Han, Z. Liu, Y. Wu, and Y. Gong, "Trajectory and Resource Optimization in OFDM-Based UAV-Powered IoT Network," *IEEE Trans. Green Commun. Netw.*, vol. 5, no. 3, pp. 1259–1270, Sep. 2021.

14. J. Zhao, J. Liu, F. Gao, W. Jia, and W. Zhang, "Gridless Compressed Sensing Based Channel Estimation for UAV Wideband Communications With Beam Squint," *IEEE Trans. Veh. Technol.*, vol. 70, no. 10, pp. 10 265–10 277, Oct. 2021.

15. E. Vlachos, C. Mavrokefalidis, K. Berberidis, and G. C. Alexandropoulos, "Improving Wideband Massive MIMO Channel Estimation with UAV State-Space Information," *IEEE Trans. Veh. Technol.*, pp. 1–14, early access, 2025.

16. C. Qing, Z. Liu, W. Hu, Y. Zhang, X. Cai, and P. Du, "LoS Sensing-Based Channel Estimation in UAV-Assisted OFDM Systems," *IEEE Wireless Commun. Lett.*, vol. 13, no. 5, pp. 1320–1324, May 2024.

17. W. Zhu, Y. Han, L. Wang, L. Xu, Y. Zhang, and A. Fei, "Pilot Optimization for OFDM-Based ISAC Signal in Emergency IoT Networks," *IEEE Internet Things J.*, vol. 11, no. 18, pp. 29 600–29 614, Sep. 2024.

18. J. Wang and S. Chen, "Deep Reinforcement Learning-Based Secrecy Rate Optimization for Simultaneously Transmitting and Reflecting Reconfigurable Intelligent Surface-Assisted Unmanned Aerial Vehicle-Integrated Sensing and Communication Systems," *Sensors*, vol. 25, no. 5, p. 1541, Mar. 2025.

19. Y. Song, Y. Zeng, Y. Yang, Z. Ren, G. Cheng, X. Xu, J. Xu, S. Jin, and R. Zhang, "An Overview of Cellular ISAC for Low-Altitude UAV: New Opportunities and Challenges," *IEEE Commun. Mag.*, pp. 1–8, early access, 2025.

20. J. Mu, R. Zhang, Y. Cui, N. Gao, and X. Jing, "UAV Meets Integrated Sensing and Communication: Challenges and Future Directions," *IEEE Commun. Mag.*, vol. 61, no. 5, pp. 62–67, May 2023.

21. W. Yuan, Z. Wei, S. Li, J. Yuan, and D. W. K. Ng, "Integrated Sensing and Communication-Assisted Orthogonal Time Frequency Space Transmission for Vehicular Networks," *IEEE J. Sel. Top. Signal Process.*, vol. 15, no. 6, pp. 1515–1528, Nov. 2021.

22. Y. Liu, I. Al-Nahhal, O. A. Dobre, and F. Wang, "Deep-Learning Channel Estimation for IRS-Assisted Integrated Sensing and Communication System," *IEEE Trans. Veh. Technol.*, vol. 72, no. 5, pp. 6181–6193, May 2023.

23. Z. Huang, K. Wang, A. Liu, Y. Cai, R. Du, and T. X. Han, "Joint Pilot Optimization, Target Detection and Channel Estimation for Integrated Sensing and Communication Systems," *IEEE Trans. Wireless Commun.*, vol. 21, no. 12, pp. 10 351–10 365, Dec. 2022.

24. Y. Liu, I. Al-Nahhal, O. A. Dobre, F. Wang, and H. Shin, "Extreme Learning Machine-Based Channel Estimation in IRS-Assisted Multi-User ISAC System," *IEEE Trans. Commun.*, vol. 71, no. 12, pp. 6993–7007, Dec. 2023.

25. Q. Zhao, A. Tang, and X. Wang, "Reference Signal Design and Power Optimization for Energy-Efficient 5G V2X Integrated Sensing and Communications," *IEEE Trans. Green Commun. Netw.*, vol. 7, no. 1, pp. 379–392, Mar. 2023.

26. X. Chen, Z. Feng, J. Andrew Zhang, Z. Wei, X. Yuan, and P. Zhang, "Sensing-Aided Uplink Channel Estimation for Joint Communication and Sensing," *IEEE Wireless Commun. Lett.*, vol. 12, no. 3, pp. 441–445, Mar. 2023.

27. K. Xu, X. Xia, C. Li, C. Wei, W. Xie, and Y. Shi, "Channel Feature Projection Clustering Based Joint Channel and DoA Estimation for ISAC Massive MIMO OFDM System," *IEEE Trans. Veh. Technol.*, vol. 73, no. 3, pp. 3678–3689, Mar. 2024.

28. X. Yang, H. Li, Q. Guo, J. A. Zhang, X. Huang, and Z. Cheng, "Sensing Aided Uplink Transmission in OTFS ISAC With Joint Parameter Association, Channel Estimation and Signal Detection," *IEEE Trans. Veh. Technol.*, vol. 73, no. 6, pp. 9109–9114, Jun. 2024.

29. K. Chen and C. Qi, "Joint Sparse Bayesian Learning for Channel Estimation in ISAC," *IEEE Commun. Lett.*, vol. 28, no. 8, pp. 1825–1829, Aug. 2024.

30. Y. Li, F. Liu, Z. Du, W. Yuan, Q. Shi, and C. Masouros, "Frame Structure and Protocol Design for Sensing-Assisted NR-V2X Communications," *IEEE Trans. Mobile Comput.*, vol. 23, no. 12, pp. 11 045–11 060, Dec. 2024.

31. C. Qing, W. Hu, Z. Liu, G. Ling, X. Cai, and P. Du, "Sensing-Aided Channel Estimation in OFDM Systems by Leveraging Communication Echoes," *IEEE Internet Things J.*, vol. 11, no. 23, pp. 38 023–38 039, Dec. 2024.

32. B. Su and M.-Y. Wang, "Joint Channel Estimation Methods in Carrier Aggregation OFDM Systems," in *Proc. IEEE 79th Veh. Technol. Conf. (VTC Spring)*, Seoul, Korea (South), May 2014, pp. 1–5.

33. C. G. Tsinos, F. Foukalas, T. Khattab, and L. Lai, "On Channel Selection for Carrier Aggregation Systems," *IEEE Trans. Commun.*, vol. 66, no. 2, pp. 808–818, Feb. 2018.

34. R. M. Rao, V. Marojevic, and J. H. Reed, "Adaptive Pilot Patterns for CA-OFDM Systems in Nonstationary Wireless Channels," *IEEE Trans. Veh. Technol.*, vol. 67, no. 2, pp. 1231–1244, Feb. 2018.

35. T. Xu and I. Darwazeh, "Transmission Experiment of Bandwidth Compressed Carrier Aggregation in a Realistic Fading Channel," *IEEE Trans. Veh. Technol.*, vol. 66, no. 5, pp. 4087–4097, May 2017.

36. Z. Wei, H. Liu, X. Yang, W. Jiang, H. Wu, X. Li, and Z. Feng, "Carrier Aggregation Enabled Integrated Sensing and Communication Signal Design and Processing," *IEEE Trans. Veh. Technol.*, vol. 73, no. 3, pp. 3580–3596, Mar. 2024.

37. Y. Li, X. Bian, and M. Li, "Denoising generalization performance of channel estimation in multipath time-varying OFDM systems," *Sensors*, vol. 23, no. 6, p. 3102, Mar. 2023.

38. X. Yang, D. Zhai, R. Zhang, L. Liu, J. Du, and V. C. M. Leung, "A Geometry-Based Stochastic Channel Model for UAV-to-Ground Integrated Sensing and Communication Scenarios," *IEEE Trans. Veh. Technol.*, vol. 74, no. 4, pp. 5307–5320, Apr. 2025.

39. M. Mirabella, P. D. Viesti, A. Davoli, and G. M. Vitetta, "An Approximate Maximum Likelihood Method for the Joint Estimation of Range and Doppler of Multiple Targets in OFDM-Based Radar Systems," *IEEE Trans. Commun.*, Aug. 2023.

40. R. Xie, D. Hu, K. Luo, and T. Jiang, "Performance Analysis of Joint Range-Velocity Estimator With 2D-MUSIC in OFDM Radar," *IEEE Trans. Signal Process.*, vol. 69, pp. 4787–4800, Sep. 2021.

41. P. Chu, Z. Yang, and J. Zheng, "Dual-Pulse Repeated Frequency Waveform Design of Time-Division Integrated Sensing and Communication Based on a 5G New Radio Communication System," *Sensors*, vol. 23, no. 23, p. 9463, Nov. 2023.

42. K. Meng, Q. Wu, J. Xu, W. Chen, Z. Feng, R. Schober, and A. L. Swindlehurst, "UAV-Enabled Integrated Sensing and Communication: Opportunities and Challenges," *IEEE Wireless Commun.*, vol. 31, no. 2, pp. 97–104, Apr. 2024.

43. P. Karpovich and T. P. Zielinski, "Integrated Sensing and Communication Using Random Padded OTFS with Reduced Interferences," *Sensors*, vol. 25, no. 15, p. 4816, Aug. 2025.

44. S. Lu, W. Yi, W. Liu, G. Cui, L. Kong, and X. Yang, "Data-Dependent Clustering-CFAR Detector in Heterogeneous Environment," *IEEE Trans. Aerosp. Electron. Syst.*, vol. 54, no. 1, pp. 476–485, Feb. 2018.